ELSEVIER

Contents lists available at ScienceDirect

Journal of Manufacturing Processes

journal homepage: www.elsevier.com/locate/manpro





Part-scale thermal evolution and post-process distortion of Inconel-718 builds fabricated by laser powder bed fusion

Qian Wang ^{a,*}, Panagiotis Michaleris ^b, Matthew Pantano ^c, Chao Li ^d, Yong Ren ^a, Abdalla R. Nassar ^c

- a Department of Mechanical Engineering, The Pennsylvania State University, University Park, PA 16802, United States of America
- ^b PanOptimization LLC, State College, PA 16801, United States of America
- ^c Applied Research Laboratory, The Pennsylvania State University, University Park, PA 16802, United States of America
- ^d Autodesk Inc., 200 Innovation Park, State College, PA 16803, United States of America

ARTICLE INFO

Keywords: Interlayer temperature In-situ Part-scale Thermal evolution Distortion Support structure

ABSTRACT

In-situ monitoring and assessment of thermal evolution during the layer-by-layer build process of a laser powder bed fusion (L-PBF) additive manufacturing system play a pivotal role to help understand the process-structureproperty correlation of the L-PBF. Interlayer temperature refers to the layer temperature after the powder is spread but before scanning a new layer commences. It represents the part heating due to the processing of the previous layers and acts as the initial temperature under which a new layer is scanned. Therefore, interlayer temperature is essential for the derivation of process control to minimize keyholes and other thermal-related defects. In addition, measurements of interlayer temperature can be used for validating part-scale thermal modeling or for detecting part defects. This paper presents an experimental study of the evolution of interlayer temperature through in-situ thermographic imaging during the fabrication of twin square-canonical parts of Inconel 718 using the EOS M280 system. Post-process distortion measurements of the fabricated parts are also obtained to provide insights into the correlation to geometric features of the part. The experimental results show that the evolution of the interlayer temperature highly correlates with the unique geometric features of the part and the support structure used to build the part. During the processing of the square-canonicals, the interlayer temperature reached as high as 325 °C, which is significantly higher than the preheated substrate temperature of 80 °C under which the first layer of the part is scanned. Measurements of the build after manufacturing show that the largest normal displacement of the part's outer wall surface reached about 17 % of its thickness. The results also show that the peak distortion and peak interlayer temperature do not occur at the same layer and are due to different causes.

1. Introduction

Laser powder bed fusion (L-PBF) is one important metal-based additive manufacturing (AM) process that enables fabrication of complex parts with a high geometric resolution [1]. In L-PBF, each layer of alloy powder is selectively melted by a laser, which is then solidified to build the part in a layer-by-layer fashion. The cycles of laser melting and rapid solidification result in large thermal gradients that could lead to a significant residual stress and distortion [2].

During the layer-by-layer build process, the evolution of the layer surface temperature reflects the spatiotemporal thermal characteristics resulted from the interaction of the geometric features of a part with repeated thermal cycles [3]. In Gouge et al. [4], *interlayer temperature* is used to refer to the temperature distribution of the layer that has just been completed and the powder has been spread, but right before the next layer is started. Hence, the interlayer temperature represents the part heating due to the processing of all previous layers and also serves as the initial temperature under which a new layer is built. The numerical part-scale thermal analysis by Li et al. [5] showed that the interlayer temperature could increase along the build direction due to heat build-up. The interlayer temperature variation could also affect melt-pool morphology. Promoppatum et al. measured thermal evolution using thermocouples at a few locations from three selected layers during the build process and showed the melt-pool morphology variation along

E-mail address: quw6@psu.edu (Q. Wang).

 $^{^{\}ast}$ Corresponding author.

the build direction [6]. Chen et al. analyzed the melt-pool morphology variation of single-scan tracks under different preheating temperatures [7]. The experimental study in [7] showed that under EOS M290's default process parameters of 285 W laser power and 1000 mm/s scan speed, the melt-pool depth increased by 31% when the preheating temperature increased from 100 $^{\circ}$ C to 500 $^{\circ}$ C, with the melt-pool depthto-width ratios falling in the transitional regime, i.e., moving from the conduction mode to the keyhole regime. Tran et al. developed P-V process maps for single-scan tracks under different initial temperature values, and demonstrated that the region of keyhole melting in the P-V process map under 400 °C had grown significantly compared to the area of keyhole melting under 80 °C [8]. This study suggested that process parameters may have to be adjusted during the layer-by-layer process to account for the changes of the interlayer temperature so that the risk of keyhole induced porosity could be reduced. Hence, in-situ monitoring of interlayer temperature during the build process could be used to provide feedback for the development of process control to improve build quality.

Furthermore, in-situ measurements of interlayer temperature could be used to validate and certify part-scale thermal models, which is a critical building block in the multi-scale thermo-mechanical analysis of L-PBF processes [4]. Part-scale thermal models have been investigated in a number of studies. For example, Dugast et al. developed a GPUbased part-scale thermal process simulator for L-PBF [9], where model-prediction on temperature contours was shown after building a representative number of grouped layers. Their part-scale thermal model prediction was validated through a block part of Ti6AL4V with a single-stripe (no contours) scanning strategy. Yavari et al. developed a mesh-free, graph-theory based part-scale thermal modeling for L-PBF [10]. To reduce computation cost, layer-scaling technique is commonly employed for part-scale modeling and simulation, e.g., by Papadakis et al. [11], Hodge et al. [12], Zaeh et al. [13], and Zhang et al. [14]. In layer-scaling, it is assumed that the heating process of a whole layer of the powder bed by the laser beam is simultaneous and furthermore, deposition of multiple physical layers is simulated by depositing a few grouped, thick layers with each grouped layer consisting of multiple physical layers. In order to validate such part-scale thermal models and to evaluate the effectiveness of layer-scaling techniques, there is a strong need for high quality, in-situ measurements of interlayer temperature. Other potential uses of in-situ monitoring of part-scale temperature evolution include correlating thermal evolution with microstructure properties [15], as well as possible detecting anomalies and defects using image recognition techniques [16,17].

Motivated by these needs, this paper presents an experimental study of the interlayer thermal evolution during the L-PBF build process, through Infrared (IR)- camera based thermographic imaging. For L-PBF, thermographic imaging has been mainly applied to the monitoring of melt-pool or heat affected zone (HAZ). Krauss et al. used a microbolometer camera, operated in the long-wave IR region, to monitor HAZ and detect deviation of process parameters, material irregularities, pores and flaws [18,19]. Lane et al. studied plasma plume and hot particle ejection from the melt region with a midwave IR camera [20]. In the study by Montazeri et al., a short-wave IR camera was used to capture thermal signatures near overhang features, which were then compared to results from a photodetector and a high-speed optical camera [21]. Foster et al. correlated IR intensities from the laser-material interaction zones to ex situ surface roughness measurements [22]. Grasso et al. used an off-axis mounted IR camera to monitor process plume from the laser melting of zinc powder and to detect unstable melting conditions [23]. Heigel et al. measured the melt-pool length and cooling rate with a short-wave IR video imaging system during the build process of 3D parts that were later used for the 2018 additive manufacturing benchmark tests [24]. These benchmark data sets were used to validate multiphysics thermal models of the build process. Lough et al. used shortwave IR imaging to monitor local thermal history and extract relevant thermal features such as melt pool area, time above threshold, and

metrics of radiance. These metrics were then used to develop empirical correlations with part properties [25]. A recent study by Baumgartl et al. applied deep-learning to the data obtained from off-axis IR monitoring to detect delamination defects and splatter [17]. Machine learning was also used by Paulson et al. to learn the correlation between local thermal history captured by the IR thermal imaging with subsurface porosity under various print conditions [26].

When thermography is used to monitor and measure the temperature distribution of a complete layer (as will be done in this paper), it requires a larger field-of-view that needs to cover the entire build area. Raplee et al. conducted a thermographic study of layer surface temperature [15] for an electron beam melting (EBM) process. The temperature profiles were used to estimate thermal gradient and solid-liquid interface, which were then correlated to microstructure of the part. For L-PBF, in-situ layerwise thermal imaging and videos have been used to capture process signatures for anomaly detection by several studies [16,27,28]. Williams et al. used a wide-field IR imaging system to study how interlayer cooling time affected the surface layer temperature and its correlation with density and grain structure variations, through a case study of building cylindrical components with different heights [29]. A similar study on the effect of interlayer cooling time was also conducted in Yavari et al. [30], where a multi-cylinder part as in [29] and an inverted cone were built, and the average temperature from IR imaging over a 9-pixel by 9-pixel region covering the center of the part was used to validate the authors' graph-theory based thermal modeling.

This study considers the interlayer thermal evolution during the L-PBF build process of twin square-canonical parts of Inconel 718. The square-canonical geometry was originally designed by the America Makes Project No. 4026 for the purpose of validating thermomechanical models for L-PBF [31]. Through thermographic imaging, a full evolution history of the interlayer temperature during the entire build process will be captured and analyzed. Post-process distortion of the outer wall surface of the final build is also measured and analyzed, to examine the correlation to geometric features of the part. The difference of this study from the existing literature is outlined in the next paragraph.

Although calibration of IR camera to capture in-situ temperature evolution was conducted before in Raplee et al. [15], it was carried out for EBM processes rather than for L-PBF. Furthermore, rather than focusing on a few layers' surface temperature to extract process signatures as done by most of the afore-mentioned layer-wise thermographic studies, this experimental study is focused on analyzing the entire evolution history of the interlayer temperature to have a holistic understanding of the thermal process and its correlation with the geometric features of the part and the support structure used to build the part. Note that how thermal history interacts with support structures has not been investigated in the afore-mentioned studies. Compared to Williams et al. [29] and Yavari et al. [30] that considered simple cylindrical components or an inverted cone, this study investigates a much more complex geometry that consists of multiple critical features including overhang surfaces built with support, varying shape/area from layer to layer, and thin-wall components. Compared to Yavari et al. [30] that focused on the average temperature obtained from a small area of the part center, this experimental study utilizes a wide-field imaging to measure interlayer temperature distribution of the entire build plate, where multiple disconnected components in the same layer experience different levels of temperature that should not be averaged. In addition to part-scale thermal evolution, this experimental study examines the correlation of post-process distortion with the geometric features of the part, for which the results may lend insight for developing thermo-mechanical simulation tools for L-PBF systems. To the best of our knowledge, this paper is the first experimental study of the interlayer temperature that is the initial temperature for melting a new layer. The in-situ sensing approach for interlayer temperature measurements developed in this paper could be used to obtain feedback for future layer-by-layer control of process parameters.

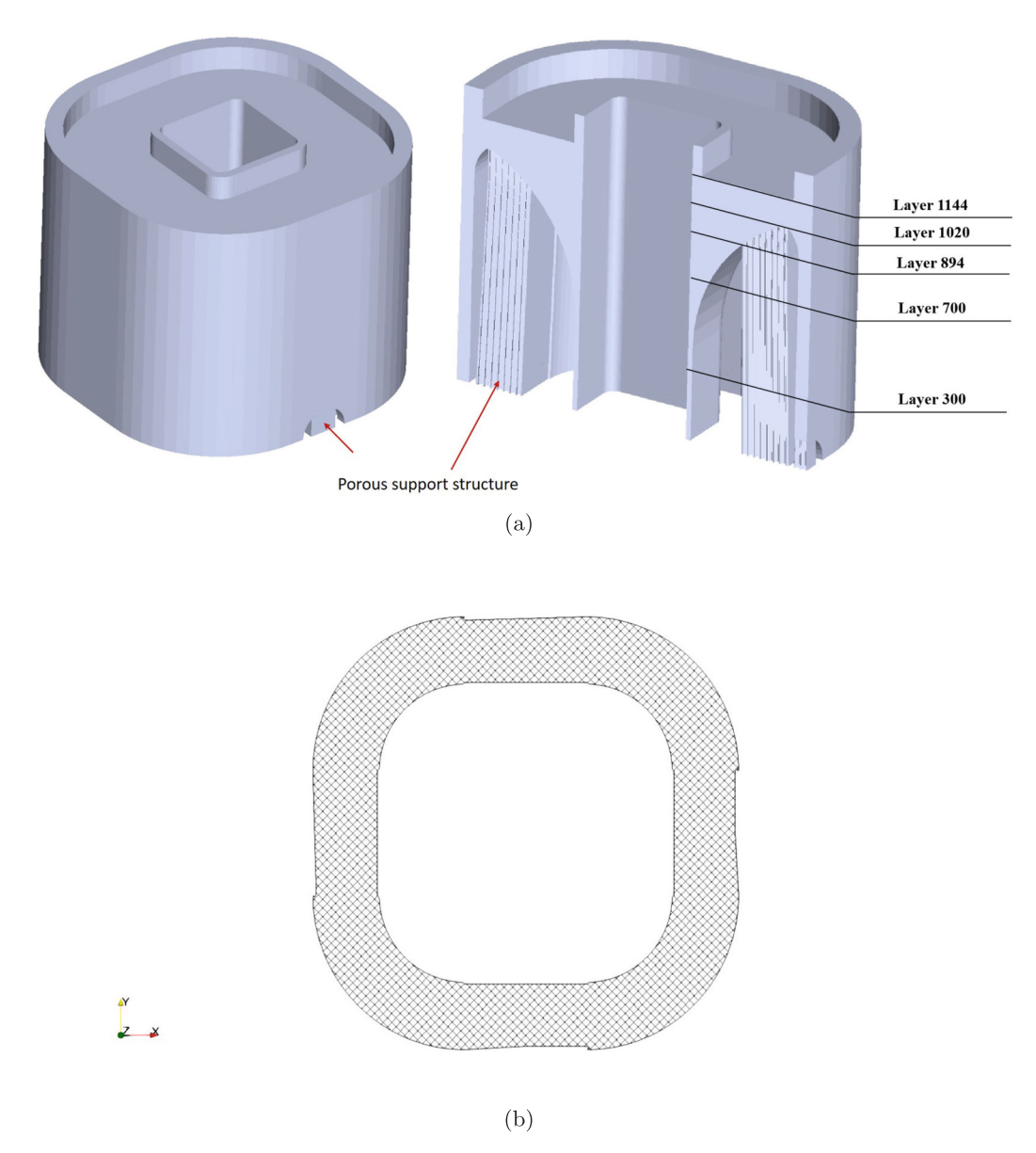


Fig. 1. (a) STL of a square-canonical geometry of 1270 layers and its mid-section view. (b) XY cross-section of the support structure.

This paper is organized as follows. Section 2 presents the methods and materials used in the experimental study. Results are given in Section 3, and conclusions are drawn in the end.

2. Methods and materials

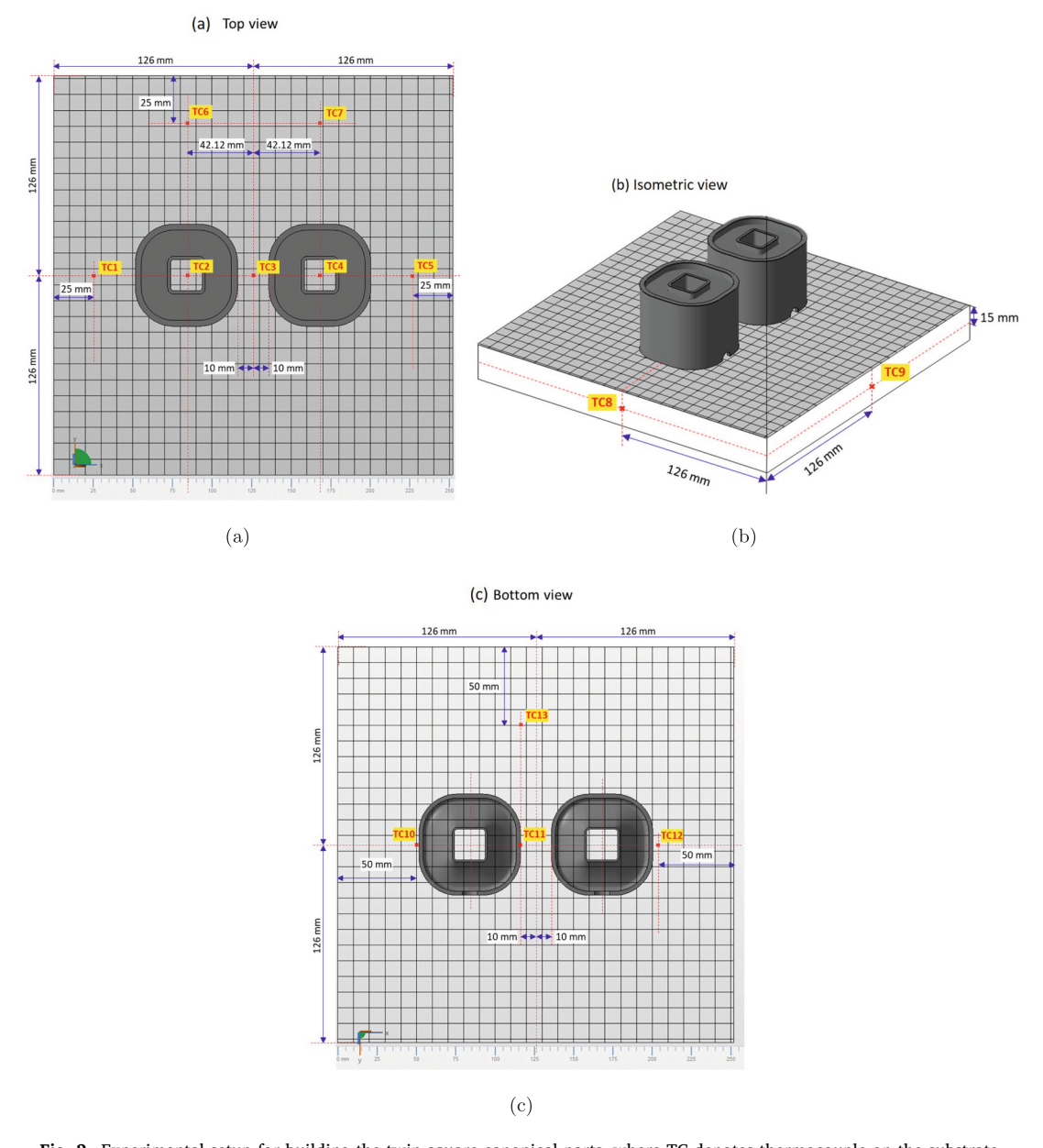
2.1. Part geometry and build configurations

The part under consideration is a square-canonical geometry, with its image in Standard Tessellation Language (STL) plotted in Fig. 1. The square of the square-canonical has a dimension of 64.24 mm \times 64.24 mm, and the part has 1270 layers with a total height of 50.8 mm. The overall dimension of the part is double the size of its original geometry from the America Makes Project No. 4026, designed for the purpose of validating thermo-mechanical models of the L-PBF process [4,31]. With twice the size, this new geometry could result in higher interlayer temperature as more heat can be accumulated in building a larger mass, and thus improve the temperature measurement resolution in this study.

The square-canonical geometry is chosen in this study due to its geometric features to create overheating and distortion. As shown in

Fig. 1, the square-canonical geometry consists of an outer wall and an inner wall. The two walls are separated at lower layers. With the increase of the layer number, the width of the inner wall keeps growing until it merges with the outer wall as a single juncture at Layer 1020, and then at Layer 1144, the two walls separate again until the end. The thickness of the outer wall is 2.29 mm before Layer 894, and the thickness of the inner wall is 0.83 mm at its early layers. It is expected that with the growth of the mass of the inner wall, heat would get accumulated but there is a lack of sufficient conduction path to transfer heat into the substrate. As a result, the final juncture, which connects the inner and outer walls to form an overhang, could create complex thermal phenomenon and result in non-negligible distortion.

As illustrated in Fig. 1(a), porous support structures of Inconel 718 are used to build the small arch at the lower-level of the geometry and to build the overhang, where the inner wall surface comes in contact with the support structure at Layer 894. The support XY cross-section shown in Fig. 1(b) is composed of square honeycomb with wall spacing of 0.82 mm and wall thickness of 0.12 mm. In terms of these dimensions, the volume fraction of the support structure, defined as the ratio of the volume of the solid component over the entire volume of the support, is



 $\textbf{Fig. 2.} \ \ \textbf{Experimental setup for building the twin square-canonical parts, where \ \textbf{TC denotes thermocouple on the substrate.} \\$

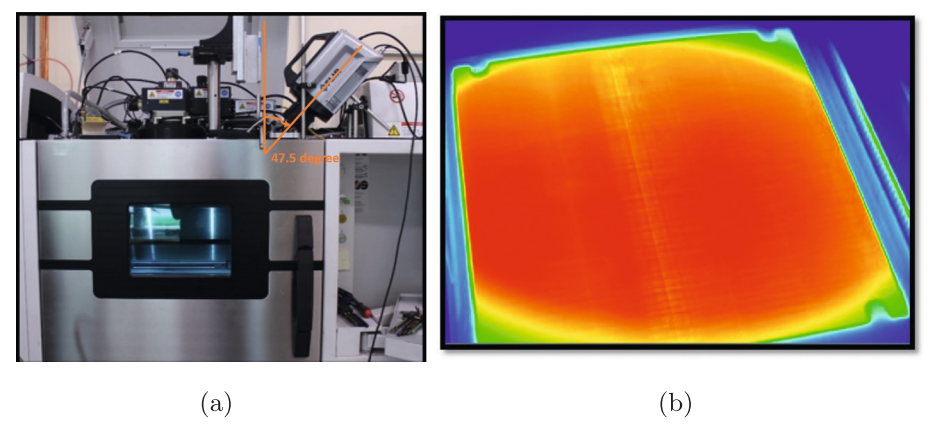
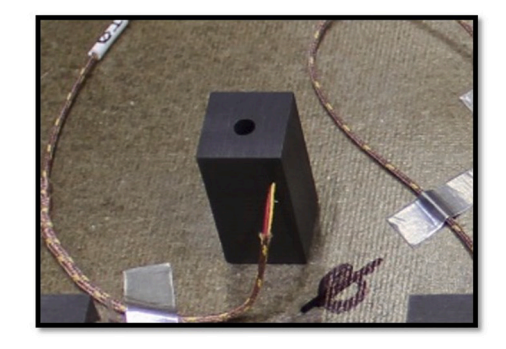


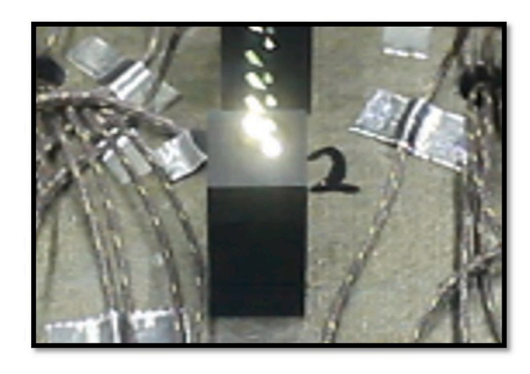
Fig. 3. System instrumentation setup. (a) FLIR mounted on top of the EOS chamber. (b) FLIR view of the build EOS platform.

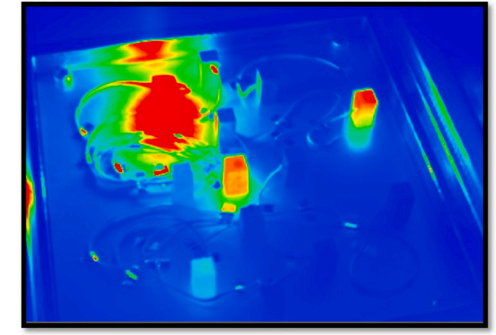




(a) Array of 13 blackbody cavities on mica plate

(b) Graphite block with 6:1 aspect ratio cylindrical cavity





(c) Heating blackbody cavities with EOS laser

(d) Thermal imaging during cool-down

Fig. 4. Blackbody calibration.

estimated to be 27 %.

In this experiment, as shown in Fig. 2, two identical square-canonical parts of Inconel 718 are built on a tool steel substrate with a dimension of 252 mm \times 252 mm \times 30 mm using the EOS M280 L-PBF system. Fabrication of two identical parts allows repeatability to account for experimental randomness. During the build process, the bottom center of the substrate is heated and maintained at a constant 80 °C, where the top surface temperature of the substrate is not directly controlled. A stripes scan strategy, with a laser power of 285 W and a scan speed of 960 mm/s, is used to build the part itself. A laser power of 100 W with a scan speed of 900 mm/s is applied to build the support structures. All scans have a hatch spacing of 110 μ m, with an initial angle of 11.5° and rotation angle of 67°. The layer thickness is 40 μ m. The recoater time for the EOS M280 machine is \sim 8.5 s. The total build time was 17 h and 30 min with a laser-on time of 14 h and 34 min.

As shown in Fig. 2, thirteen K-type thermocouples (TC) are placed on the substrate to measure the in-situ temperature changes at various locations of the substrate. Among them, seven thermocouples (TC1–TC7) are located at the top of the substrate (embedded in the substrate with the junctions exposed on the top surface), two (TC8 and TC9) located at the side, and four (TC10–TC13) located at the bottom of the substrate.

2.2. In-situ system instrumentation and calibration

2.2.1. Camera setup

Fig. 3 illustrates the system instrumentation for the in-situ thermographic data collection to measure the interlayer temperature. Recall that interlayer temperature is the layer-wise top-surface temperature distribution right after each layer has just been completed and the recoater has swept past, but right before the next layer is started. A midwave IR camera, FLIR X6801sc, is mounted on top of the EOS chamber with an angle of 47.5° between the camera's axis and the surface normal. It has a direct view of the substrate through the chamber top viewport. A 6 mm-thick zinc selenide window, with transmission

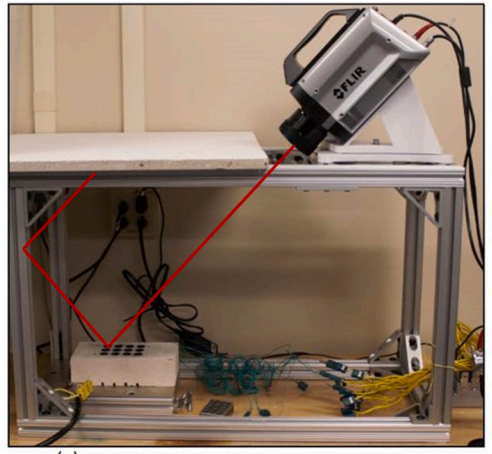
larger than 95 % at 3–5 μm wavelength, is used at the viewport. The camera calibration accounts for all external optics including the viewing optics. For this study, images of the powder bed area were captured at a resolution of 332 \times 480 pixels (~670 μm per pixel). Using a calibration grid and the MATLAB Camera Calibrator application, a projective 2D transformation was applied to project the IR data onto a 2500 \times 2500 pixel image in the same plane as the powder bed.

The FLIR camera imaging has a spectral range of 3–5 μm , with factory calibrations from $-20\,^{\circ}\text{C}$ to 350 $^{\circ}\text{C}$ for its 25 mm lens with no filter. In addition, FLIR uses a superframing technique, which varies the integration time of the camera from frame to frame and then produces a composite superframe of four presets, covering 10–90 $^{\circ}\text{C}$, 35–150 $^{\circ}\text{C}$, 80–200 $^{\circ}\text{C}$, and 150–350 $^{\circ}\text{C}$, respectively. The time interval between two consecutive frames is about 25 ms, during which the change in interlayer temperature distribution is negligible. This is due to that interlayer temperature is measured after a layer of powder being spread, and thus at that time, there is no moving heat source with which the temperature distribution would be rapidly changing.

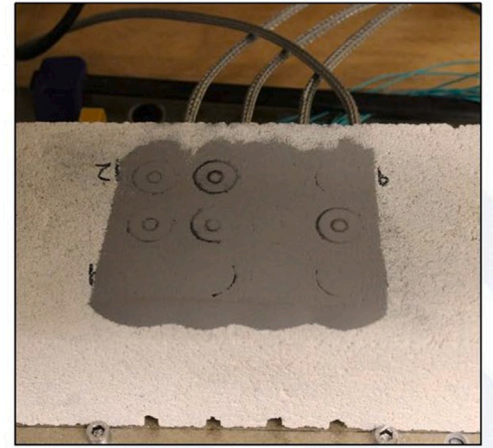
2.2.2. Calibration

Calibration of a thermal camera refers to the process of correlating the infrared radiation measured by the camera with known temperatures. Despite the factory calibration conducted by the FLIR manufacturer, two types of calibration, including a blackbody calibration and a material emissivity calibration, are further conducted to improve the accuracy of converting the IR intensity taken during the build process to the temperature outputs.

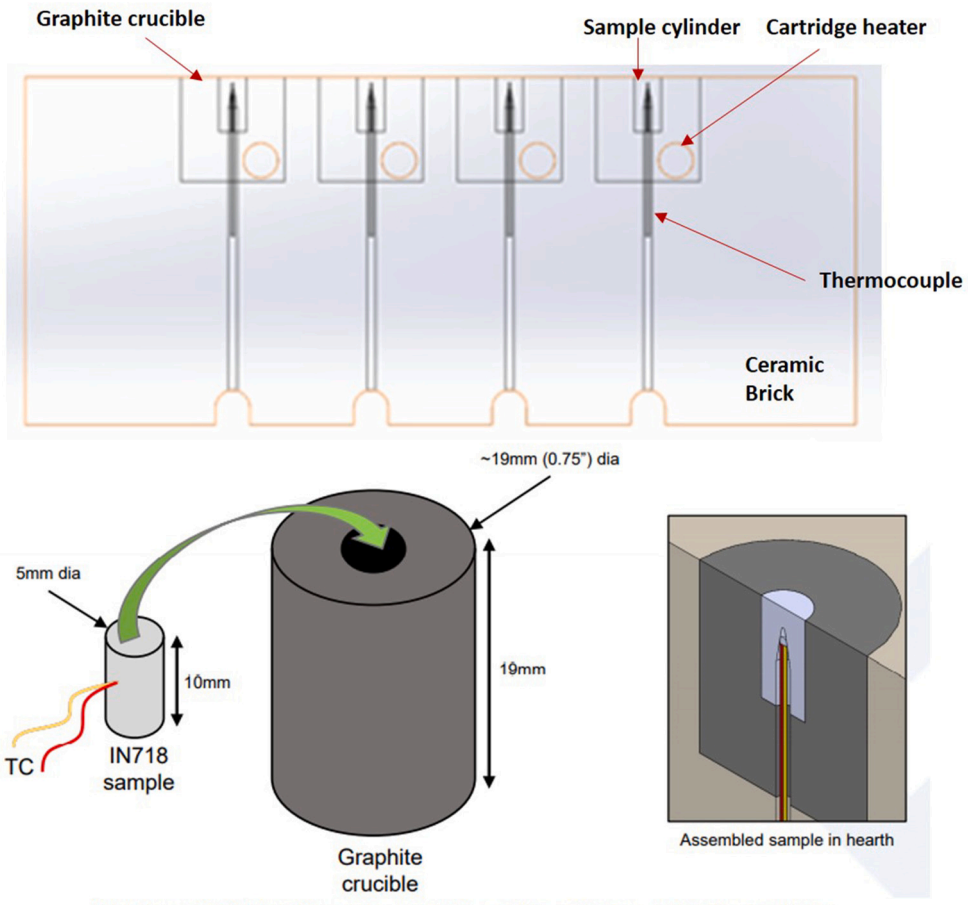
2.2.2.1. Blackbody calibration. Blackbody calibration is commonly performed under controlled conditions in a specialized lab by the camera manufacturer using a number of blackbody reference sources. Blackbody reference sources typically have an emissivity greater than 0.985. By the Sakuma-Hattori formula [32], the thermal radiance $L^{\rm D}_{\Omega}$ emitted from a perfect blackbody is computed in terms of its







(b) Hearth with powder-coated samples (top view)



(c) Schematic illustration of hearth with sample cylinders and thermocouples

Fig. 5. Experimental setup for emissivity calibration.

temperature T as follows:

$$L_{\Omega}^{b}(T) = \frac{R}{exp(B/T) - 1} \tag{1}$$

where R and B are model parameters that need to be calibrated. In this experimental study, blackbody calibration is conducted to correct for variations caused by instrumentation setup, including corrections for spatial variation in flux density due to camera perspective, and corrections for thermal filtering effects and temperature contribution from external optics.

Fig. 4 illustrates the blackbody calibration experiment. An array of

blackbody cavities are placed on the imaging plane in 13 locations inside the EOS chamber. Each blackbody cavity consists of a small graphite block having a cylindrical hole with an aspect ratio of 6:1. In terms of the 6:1 aspect ratio and the wall emissivity of 0.75 [33], the effective emissivity of the cylindrical cavities is estimated to stay between 0.987 and 0.997, according to different computation models given in the work by Quinn [34]. Thermocouples are embedded in the graphite targets to measure the reference temperatures. The blackbody cavities are then heated to over 350 °C sequentially by the EOS process laser, with a laser power of 50 W and scan speed of 1750 mm/s. Synchronized IR imaging and thermocouple data are recorded during the cool-down period for calibration. Then the collected radiance and temperature data at each

TC location are fitted to the Sakuma-Hattori model in Eq. (1), which calibrates the model parameters R and B for each pixel and for each preset. The resulting coefficient of determination for the model fit is $R^2 = 0.9999$.

2.2.2.2. Material emissivity calibration. Emissivity is conventionally defined as the ratio of the radiance emitted by a flat, opaque, and optically smooth surface to the radiance emitted by a perfect blackbody cavity, at a given temperature and wavelength [35]. Strictly speaking, emissivity is an intrinsic material property. Some references use the word *emittance* to refer to the effective emissivity of a material with a nonflat or non-smooth surface [15,36]. However, in this paper, by relaxing the notation a bit, we use emissivity to describe the ratio of the radiant flux emitted by non-flat, non-smooth, real surfaces relative to the radiant flux emitted by a blackbody at the same temperature.

The total radiance observed when viewing a surface (denoted by L_{Ω}) is the sum of radiance emitted from the surface (denoted by L_{E}) and the radiance from the surroundings reflected by the surface (denoted by L_{R}) [37]:

$$L_{\Omega} = L_E + L_R \tag{2}$$

where L_E at a surface temperature T_s can be computed in terms of the emissivity of the material surface, ε_{Ω} , and the radiance of a perfect blackbody L_{Ω}^b at the surface temperature T_s as follows:

$$L_E = \varepsilon_{\Omega} \cdot L_{\Omega}^b(T_s) \tag{3}$$

Furthermore, assuming that the surroundings are isothermal, the reflected radiance L_R at the surrounding temperature T_{SUTT} can be computed as follows:

$$L_R = (1 - \varepsilon_{\Omega}) \cdot L_{\Omega}^b(T_{surr}) \tag{4}$$

It is easy to verify that for a blackbody ($\varepsilon_{\Omega}=1$), $L_{\Omega}=L_{E}=L_{D}^{b}$, i.e., L_{Ω} reduces to the blackbody radiance given in the Sakuma-Hattori formula in Eq. (1).

By Eqs. (2)–(4), the emissivity of the surface of a specimen can be derived as follows:

$$\varepsilon_{\Omega} = \frac{L_{\Omega} - L_{\Omega}^{b}(T_{sur})}{L_{\Omega}^{b}(T_{s}) - L_{\Omega}^{b}(T_{sur})} \tag{5}$$

which is a function of the total radiance observed by the IR camera, the surface temperature T_s , and the surrounding temperature T_{SUUT} . The calculation of the function $L^b_{\Omega}(\cdot)$ is given in Eq. (1).

For an EBM process, the study by Dinwiddie et al. reported that the effective emissivity (emittance) of Inconel 718 sintered powder stayed at a constant $\varepsilon=0.68$ for temperature in the range of 800 °C–1275 °C, and the emittance of the as-printed Inconel surface was 0.37 at 800 °C, then increased linearly with temperature, and finally reached to 0.46 at 1275 °C [36]. Similarly, Raplee et al. conducted respective IR intensity-to-temperature calibration for the powder and as-printed Inconel 718 in their study for EBM, where the calibration curve was switched from the powder case to the as-printed case in processing the temperature data when melting was deemed to occur [15]. In this study, noting that interlayer temperature corresponds to the layer surface temperature right after the recoater has swept past, i.e., the in-situ measurements are performed on a 40–60 μ m powder layer atop as-printed Inconel 718, rather than directly on the bare part.

The effective emissivity calibration is conducted through a dedicated test stand simulating the FLIR position on EOS, as illustrated in Fig. 5. The experimental setup is shielded in the directions of the first and second reflections to block reflected IR radiance from warm sources in the room (Fig. 5(a)). The ceramic-brick hearth houses a total of 12 samples in three rows, with four samples in each row. Each sample is an as-built EOS Inconel 718 cylinder coated with a 40–60 μ m thick layer of Inconel 718 powder, and it is buried in a graphite crucible for heating. A

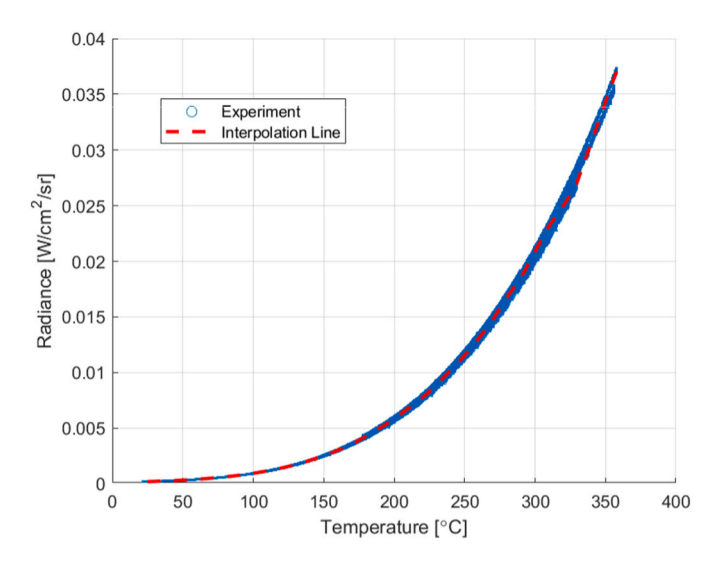


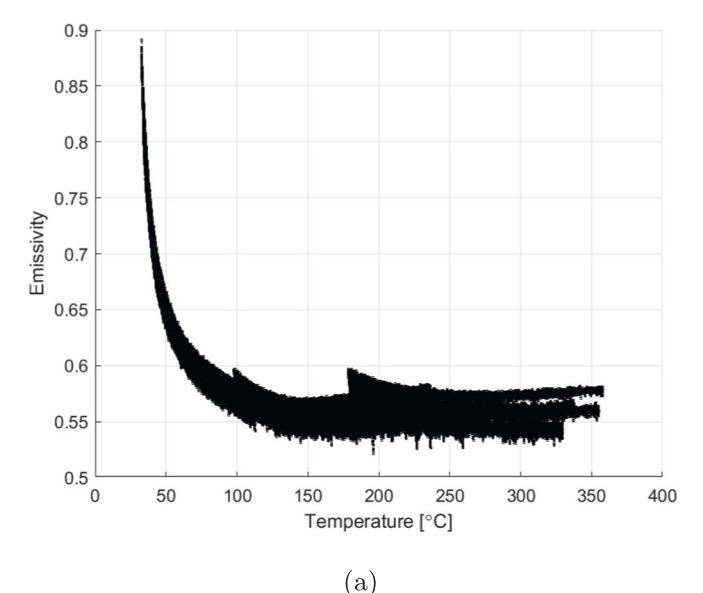
Fig. 6. Observed IR radiance versus TC data in the calibration experiment. The dashed line connects all pairs of (TC temperature, mean radiance) for all TC values.

dedicated type-K thermocouple is buried just below the surface of each sample to measure the reference temperatures.

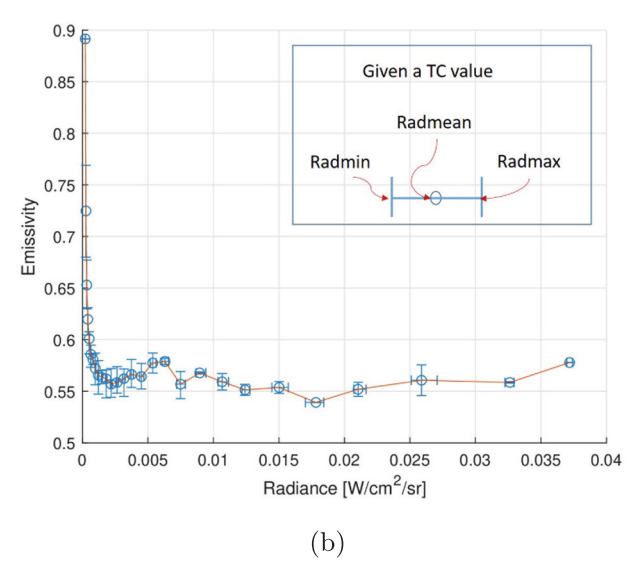
In the calibration experiment, the 12 samples in the hearth are heated electrically through cartridge heaters to 350 °C (the highest temperature where the camera is factory calibrated) and then allowed to cool to the room temperature of 22.25 °C. No oxidation effect was detected for the samples after reaching the highest temperature. Synchronized IR imaging and thermocouple data have been recorded during the cool-down period for calibration. At each TC value, a small region of interest is created in the image of each sample, from which the max, min, and mean pixel-radiance values are extracted. Fig. 6 plots all observed IR radiance with respect to temperatures measured by each TC, for all TCs. The dashed line is derived by applying 1-D data interpolation (MATLAB command *interp1*) to all pairs of (TC temperature, mean radiance) for all TC values.

For a surrounding temperature $T_{surr}=22.25~^{\circ}\text{C}$, by Eq. (5) and the radiance-temperature relationship obtained from the calibration experiments (Fig. 6), the material emissivity ε_{Ω} as a function of the surface temperature can then be computed, for which Fig. 7(a) shows the resulting scatter plot. It is worth pointing out that by Eq. (5), when the surface temperature $T_s \rightarrow T_{surr}$, it will lead to $\varepsilon_{\Omega} \rightarrow \infty$, which implies that the calculation of the emissivity is no longer valid when $T_s \rightarrow T_{surr}$. By further computing the derivatives of the mean emissivity curve (not shown here, corresponding to a smoothed mean-line extracted from the scatter plot in Fig. 7(a)) using a finite-difference approximation, an inflection point at \sim 50 $^{\circ}$ C is identified, below which Eq. (5) is deemed not applicable to compute a reliable emissivity value.

Using Fig. 7(a) together with Fig. 6, the emissivity ε_Ω as a function of the IR radiance is then derived, which will then be used to convert the IR radiance to temperature outputs in Method B of Section 2.3. Recall that in the emissivity calibration experiment, for each TC value, a small region of interest is created in the image for each sample, from which the max, min, and mean pixel-radiance values are extracted. They are denoted by Radmax, Radmin, and Radmean in the inset of Fig. 7(b), which explains how the horizontal error bars are derived. For clarity in showing the error bars, only a small portion of the data sets obtained from the emissivity calibration experiment are shown in Fig. 7(b), with the full data sets shown in Fig. 7(c). The red solid line in Fig. 7(b) is drawn by connecting all Radmean values.



(α,



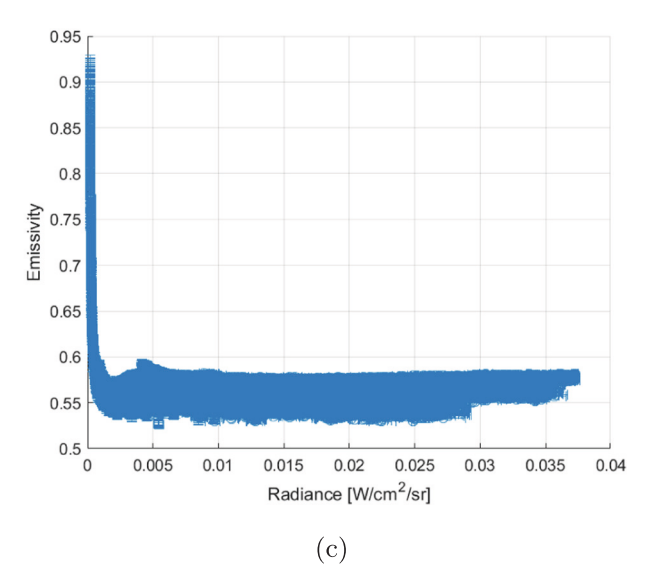


Fig. 7. (a) Emissivity with respect to temperature; (b–c) derived emissivity with respect to IR radiance. Only a portion of the data sets are shown in (b) for clarity in viewing the error bars, where the inset shows that for a given TC value, the max and min radiance are obtained to define the horizontal error bar; all data sets are shown in (c). (For interpretation of the references to color in this figure, the reader is referred to the web version of this article.)

2.3. Data processing

After calibration, two approaches are used to process the thermographic radiance data to derive the corresponding temperature outputs. The first approach (referred to as Method A) computes the temperature outputs through a lookup table built directly from the IR radiance-to-temperature curve in Fig. 6. The second approach (referred to as Method B) computes the temperature outputs using the derived radiance-dependent emissivity shown in Fig. 7(b).

2.3.1. Method A: through table lookup

First, a lookup table is built to represent the functional relationship from the IR radiance to the surface temperature. Fig. 6 shows the raw experimental data from calibration, with radiance in the range of $[1.7698\times10^{-4}, 0.0374]$ W/cm²/sr. Recall that the dashed line is derived by applying 1-D interpolation to all pairs of (TC temperature, mean radiance). By flipping the *x*-axis and *y*-axis of Fig. 6, the dashed line in Fig. 6 represents the lookup table for the surface temperature as a function of IR radiance. For any given radiance value shown in Fig. 6,

the standard deviation of the corresponding temperature is less than 6 °C, which provides a quantification of the temperature uncertainty resulting from using Method A.

2.3.2. Method B: through radiance-dependent emissivity

Note that the Sakuma-Hattori formula in Eq. (1) is only for black-bodies. For all other bodies, the IR camera measures the radiance that is only a fraction of the true surface temperature. By combining Eqs. (1) and (3),

$$L_{E} = \varepsilon_{\Omega} \cdot \frac{R}{exp(B/T_{s}) - 1} \Rightarrow T_{s} = \frac{B}{ln(\frac{R}{L_{E}/\varepsilon_{\Omega}} + 1)}$$
 (6)

by Eq. (2), L_E also satisfies

$$L_E = L_{\Omega} - (1 - \varepsilon_{\Omega}) L_{\Omega}^b(T_{surr}) \tag{7}$$

Then, the surface temperature T_s is derived by combining Eqs. (6) and (7) as follows:

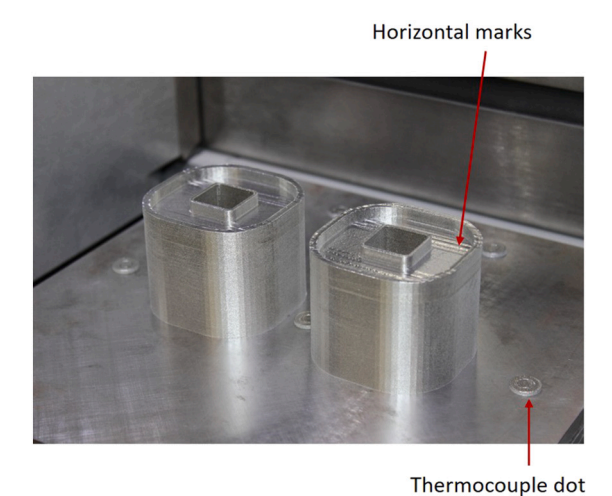


Fig. 8. Image of the final build.

(a) TCs located on the top surface of substrate

$$T_{s} = \frac{B}{ln\left[\frac{\varepsilon_{\Omega} \cdot R}{L_{\Omega} - (1 - \varepsilon_{\Omega}) L_{\Omega}^{b}(T_{surr})} + 1\right]}$$
(8)

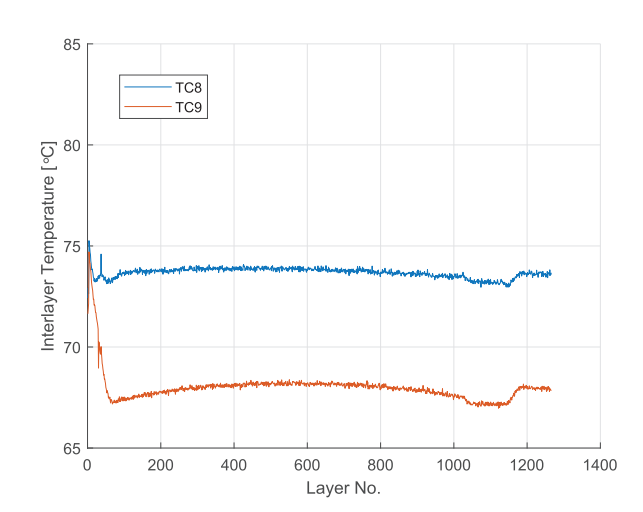
where the emissivity ε_Ω is radiance-dependent. Note that although error bars are shown in Fig. 7(b) for the radiance-dependent emissivity, only mean values of the radiance-dependent emissivity are used in Eq. (8) to compute the temperature outputs here.

3. Results

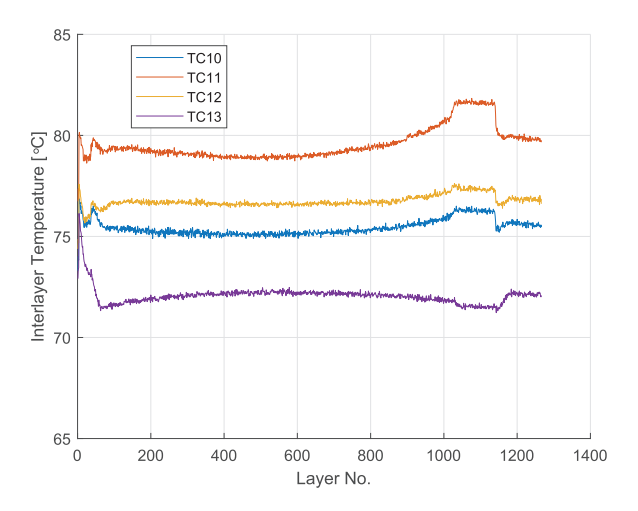
Fig. 8 shows the image of the final build. The thermocouple dots next to the square-canonical parts were originally designed to estimate material emissivity during the build process and they were incorporated into the build process of the first 40 layers. However, as the temperature values of the hot powder in the first 40 layers are not sufficiently higher than the surrounding temperature and they do not help with calibration under high temperature, the resulting emissivity estimation is not used in data processing in this paper and the related details are omitted here.

3.1. In-situ thermocouple measurements on substrate

The in-situ temperature histories measured by TC1-TC13 on the substrate are given in Fig. 9. As the bottom center of the substrate is set



(b) TCs located on the side of substrate



(c) TCs located on the bottom of substrate

Fig. 9. In-situ temperature evolution on the substrate.

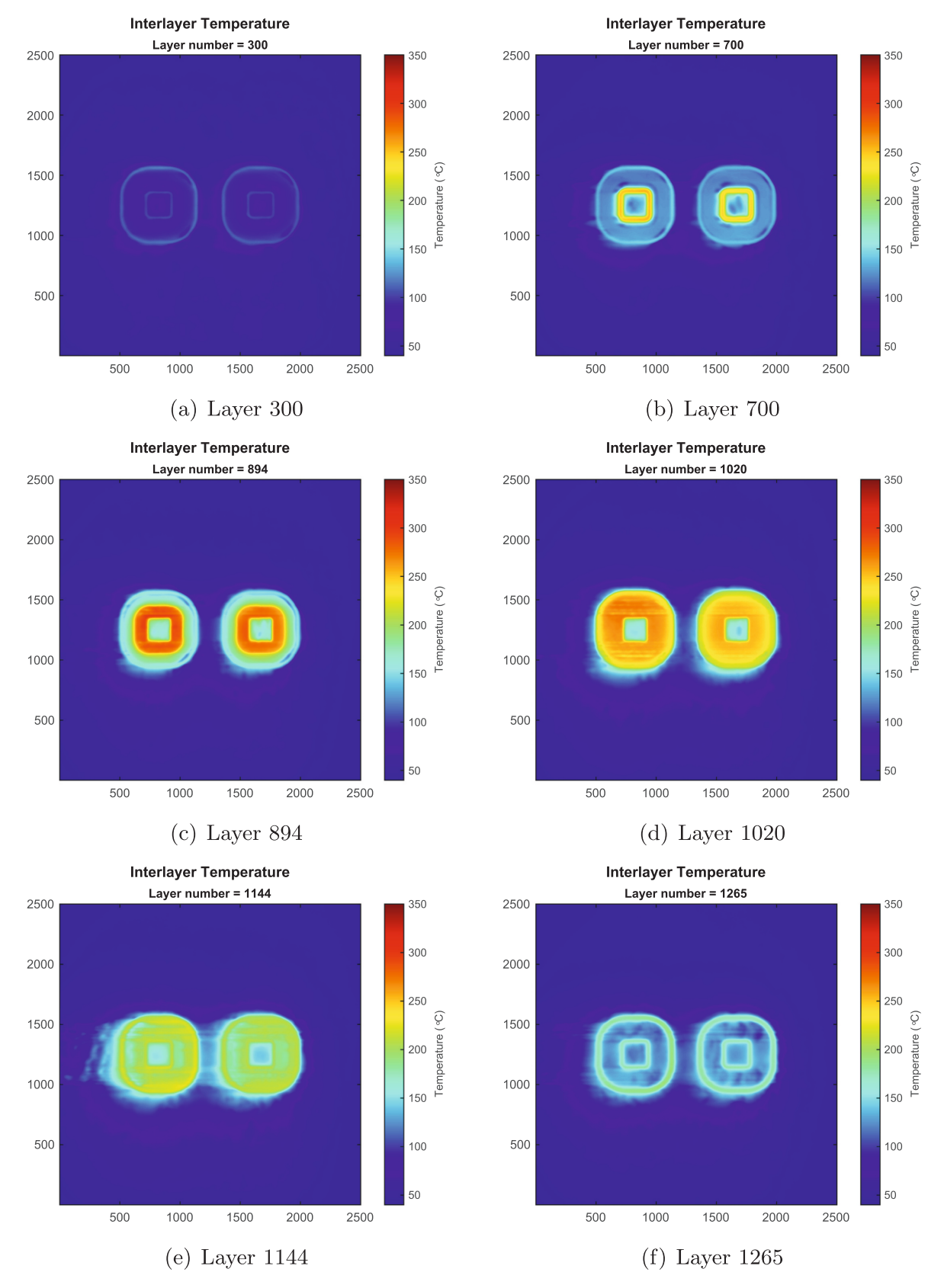


Fig. 10. Interlayer temperature distribution at selected layers, where IR radiance is converted to temperature using Method A.

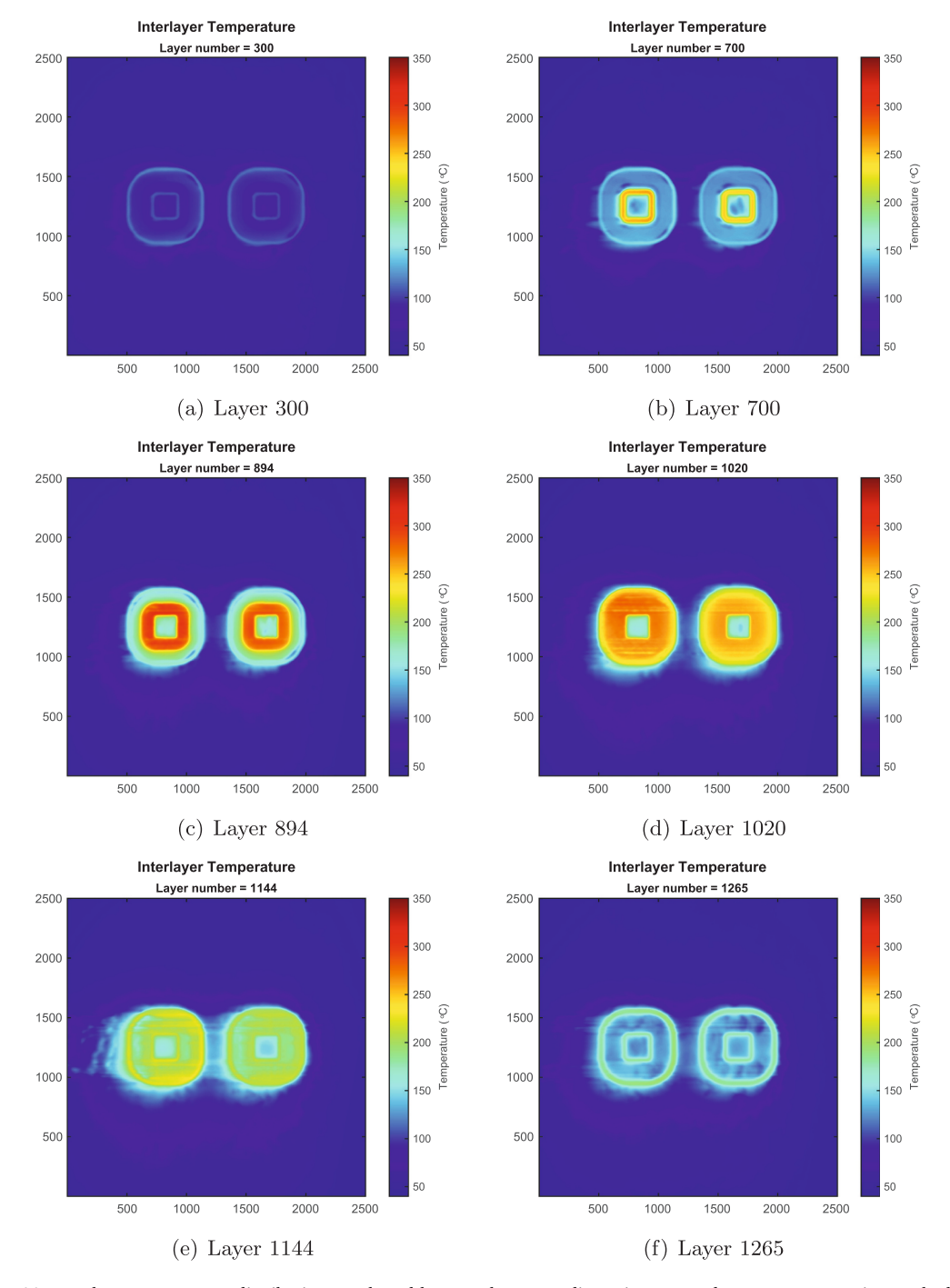


Fig. 11. Interlayer temperature distribution at selected layers, where IR radiance is converted to temperature using Method B.

to 80 °C, the time histories of TC2–TC4 and TC11 are around 80 °C, with other TCs, located further away from the center, having temperature at a few degrees lower than 80 °C. It is also observed that the temperatures of TC2–TC4 and TC11 have reached their respective peak values within layers 1000–1200, where the inner wall merges with the outer wall to form an overhang.

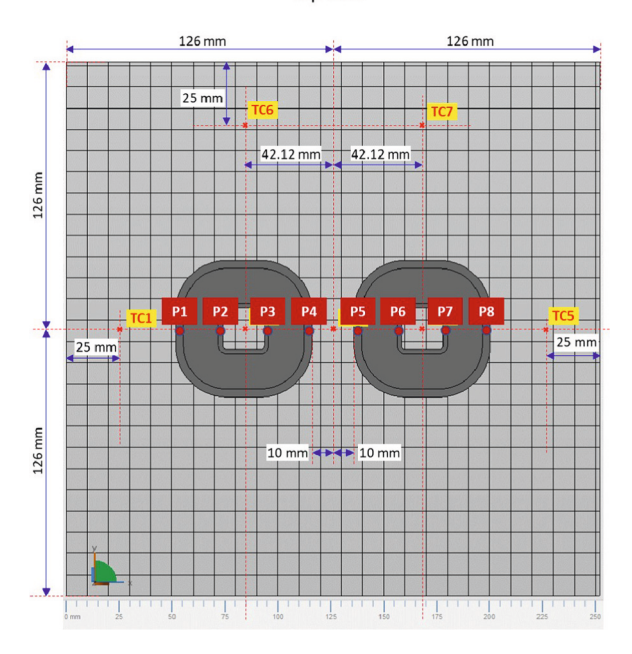
3.2. Interlayer temperature

The reader can refer to the videos for the entire evolution of interlayer temperature in the Supplemental material section available online. The observed IR radiance values of interlayer temperature ranged in [1.8388×10^{-4} , 0.0290] W/cm²/sr, well within the range of radiance

values of $[1.7698\times10^{-4},\ 0.0374]\ \text{W/cm}^2/\text{sr}$ from the calibration experiment (Fig. 6). Figs. 10 and 11 show the interlayer temperature distribution at several representative layers: layer 300, 700, 894, 1020, 1144, and 1265. For Fig. 10, Method A in Section 2.3 is used to convert the IR radiance to temperature, whereas in Fig. 11, Method B is used to compute temperature values from the IR radiance.

At Layer 300, the inner and outer walls remain separate but the thickness of the inner wall has increased compared to its initial layer. Note that the temperatures of the inner and outer walls are close to each other at this layer. At Layer 700, the inner wall is much hotter than the outer wall, as the mass of the inner wall has kept increasing for many layers (see Fig. 1(b)) but there is not sufficient path for the accumulated heat to conduct into the substrate. At Layer 894, the inner-wall

Top view



(a) Selected point locations

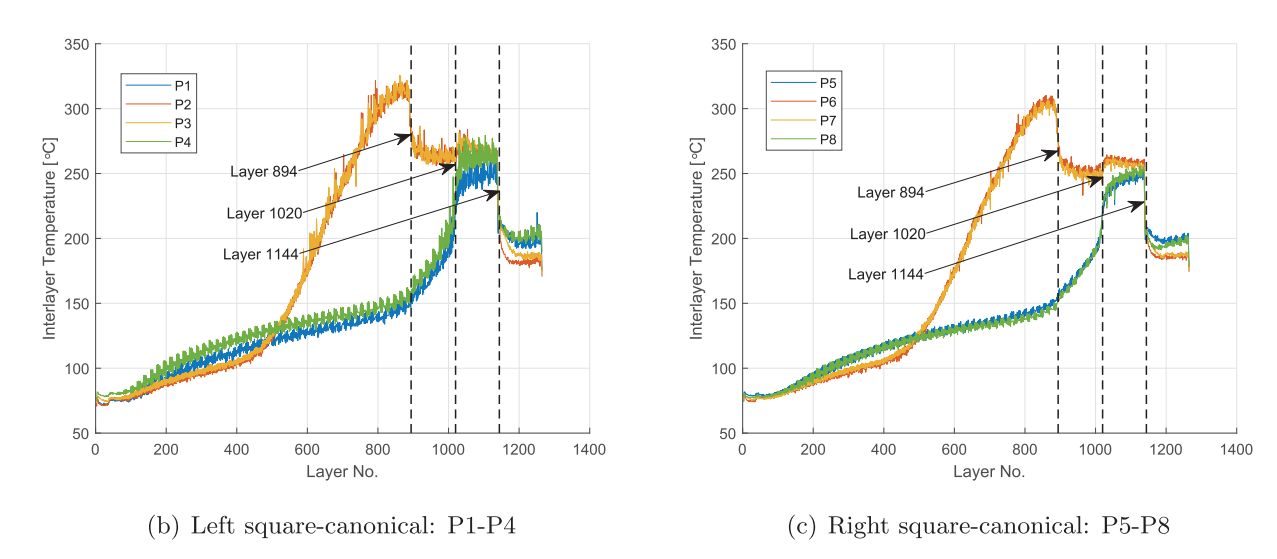


Fig. 12. Temperature evolution at several sample locations across all layers (Method A).

temperature is close to its peak value and it is significantly higher than the temperature of the outer wall. At Layer 1020, the inner wall starts to merge with the outer wall to form a single juncture, raising up the temperature value of the outer wall, but the inner wall temperature at this layer is lower than that at Layer 894. At Layer 1144, inner and outer walls start to separate again, further reducing the temperature of each wall. At Layer 1265, which is close to the end of the build, the inner and outer walls remain separated and have similar interlayer temperature.

The time evolution of the interlayer temperature of the left square-canonical resembles its right counterpart. However, the left canonical part appears to be slightly hotter than the right one at the same layer. This could be partially due to that the recoater blade sweeps from right to left, carrying heat through powder from right to left. The trail of warm powder can be seen in many frames as a warm shadow to the left of each canonical part, as shown in Figs. 10(c)–(f) and 11(c)–(f). The temperature difference between the left and right parts is more pronounced at the inner wall of the part. This may be attributed to that inner wall is

surrounded by powder and has limited heat transfer path to the substrate, thus showing accumulated energy transferred through the powder spreading of all previous layers.

Figs. 12 and 13 further examine the temperature evolution at several selected sample locations on the walls during the build process. Four sample locations are picked from each square-canonical part, and for each part, two locations are chosen from the outer wall (P1/P4 and P5/P8) and two locations are chosen from the inner wall (P2/P3 and P6/P7). The sample points are located at the mid-ways of the thickness of the inner or outer wall. The temperatures in Fig. 12 are derived using Method A to process the IR radiance, and the temperatures in Fig. 13 are derived using Method B. Figs. 12–13 show that the interlayer temperature has reached as high as 325 °C, which is significantly higher than the preheated substrate temperature of 80 °C under which the first layer of the part is scanned.

It can be seen that before approximately Layer 500, the temperature at P2/P3 (or P6/P7) of the inner wall stays close to the temperature at

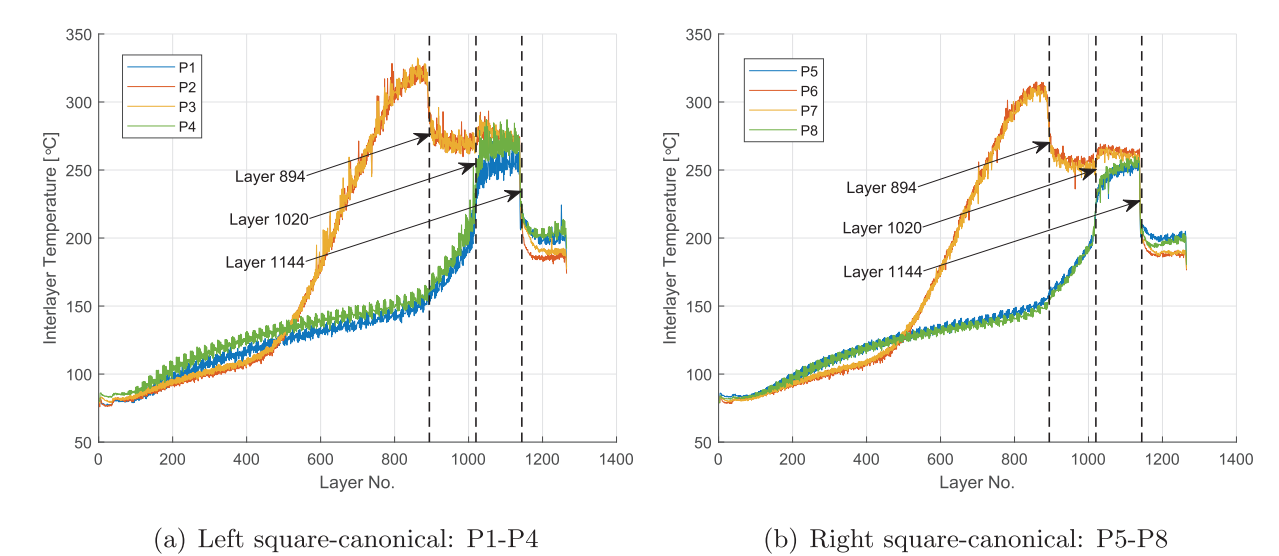


Fig. 13. Temperature evolution at several sample locations across all layers (Method B).

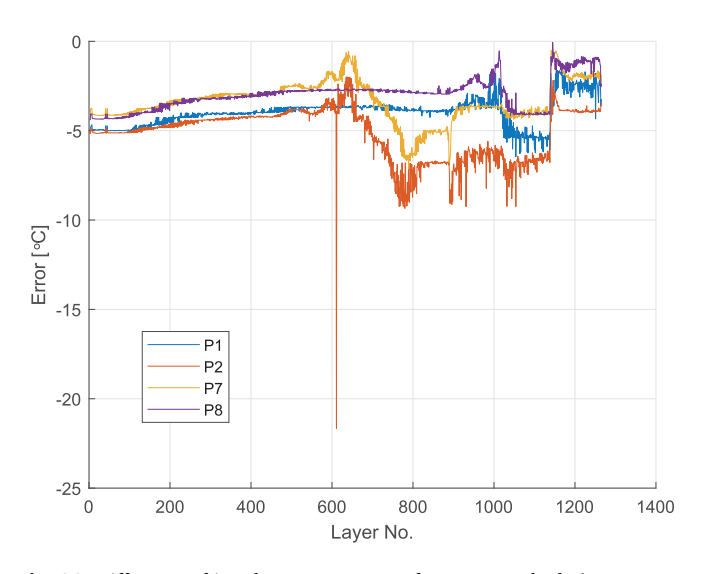


Fig. 14. Difference of interlayer temperature from two methods (temperature from Method A minus temperature from Method B) at selected locations: P1 and P2 on the left square-canonical, and P7 and P8 on the right square-canonical.

P1/P4 (or P5/P8) of the outer wall, in the range of 110 °C-130 °C. Afterwards, the temperature of the inner wall starts to surpass that of the outer wall. The temperature at the inner wall locations (P2/P3 or P6/P7) reaches its peak value within the range of 300 °C-325 °C before Layer 894. The peak inner wall temperature is about 160 $^{\circ}\text{C}$ higher than the temperature of the outer wall (at locations P1/P4 and P5/P8) in the same layer. Note that the inner wall surface comes in contact with the support structure at Layer 894 (see Fig. 1(b)), providing an additional path to transfer the heat to the substrate. This leads to a sudden drop in temperature of the inner wall, which eventually merges with the temperature of the outer wall at about 250 °C. The thickness of the outer wall starts to grow after Layer 894 (see Fig. 2), which contributes to the rapid increase of temperature of the outer wall after Layer 894. The outer wall merges with the inner wall at Layer 1020, causing the sudden temperature rise for the outer wall. At Layer 1144, the two walls separate again and both temperatures have dropped to the range of 180 °C–210 °C. By examining the entire build process, the evolution of the interlayer temperature is demonstrated to not only correlate with the critical geometric features of the part but also correlate with the location of the support structure.

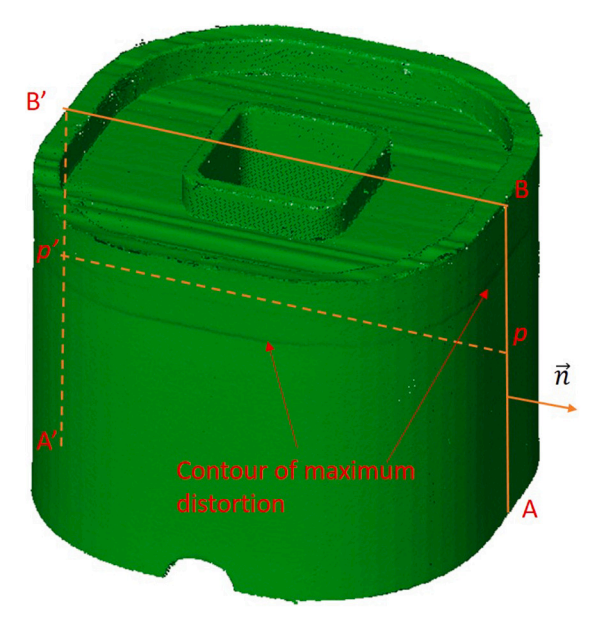


Fig. 15. Image of the scanned part generated from point cloud data. Sample paths AB and A'B' are selected to measure normal displacement and distortion, where \overrightarrow{n} denotes the normal vector of the outside surface along which the normal displacement is defined.

The measured temperatures of the left square-canonical appear to be more noisy than its right counterpart. The influence of the trail of warm powder could be one contributing factor. It is also observed that the temperature at P4 is always higher than the temperature at P1 for any layers, in spite of the afore-mentioned influence of the warm powder trail. In addition, the temperature at P5 is in general higher than the temperature at P8. The higher temperatures at P4/P5 may be attributed to that the proximity of the two canonicals has caused thermal interaction.

The difference of the interlayer temperature between Method A and B at several selected locations is given in Fig. 14. It can be seen that for all layers, the difference between the two methods is less than 10 $^{\circ}\text{C}$ except a single outlier of 25 $^{\circ}\text{C}$ occurred slightly after Layer 600. The outlier may be attributed to the large emissivity variance at about 180 $^{\circ}$ as shown in Fig. 7(a), which is used in Method B. In contrast, Method A has bypassed estimating emissivity and thus avoided any discrepancy

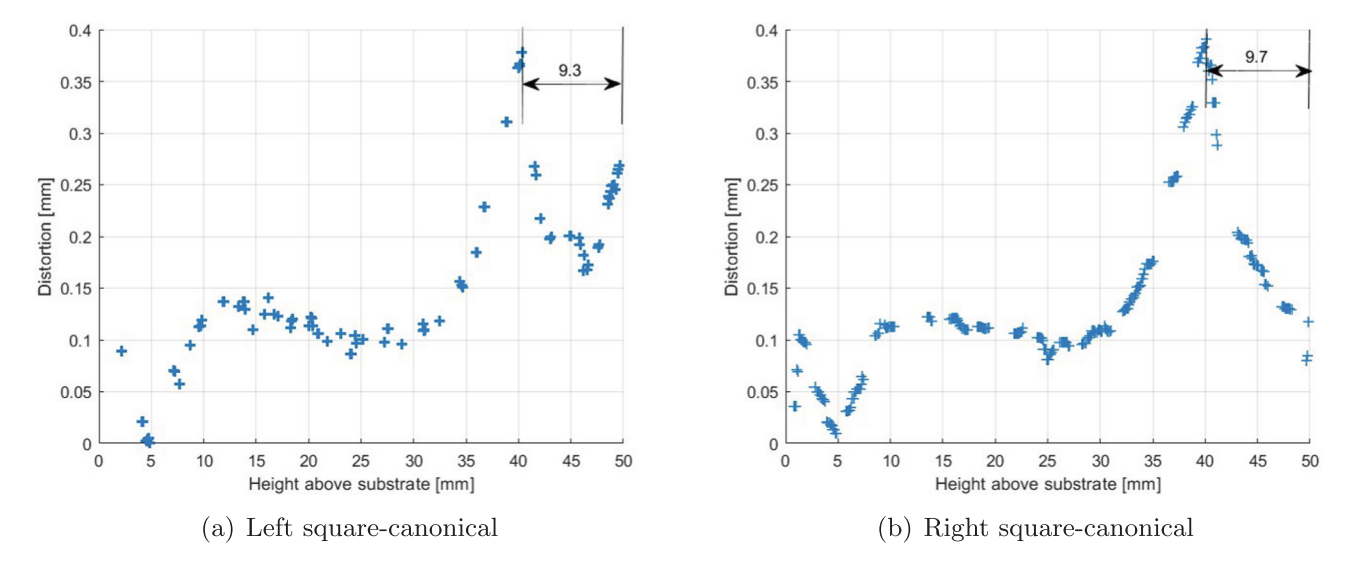


Fig. 16. Normal distortion with respect to height above the substrate, along the sample paths shown in Fig. 15. The average height of the final part being scanned is 50.22 mm.

that may be caused by uncertainty in estimating emissivity. Due to the overall small difference between the two methods, when an explicit estimation of the effective emissivity is not needed, Method A is considered a simple and convenient approach to converting IR radiance measurements to the temperature outputs.

3.3. Part distortion

After manufacturing is completed, the square-canonical parts are removed from the substrate and then scanned by a FARO Edge coordinate measuring machine (CMM) (2.7 m, seven axis) coupled with a FARO Laser Line Probe ES with ± 0.041 mm volumetric accuracy [38], by which the deformed outside surface is measured. It is acknowledged that stress relaxation from the substrate removal affects distortion. However, the effects of thermal history and part geometry on distortion are still easily discernible. Fig. 15 plots one scanned canonical part from the point cloud data for illustration. In this section, the sample paths AB and A'B' are selected to illustrate the normal displacement and distortion, where the plane of ABB'A forms a mid-section cut of the squarecanonical geometry. The average height of the final part is measured as 50.22 mm using a Mitutoyo 293-342-30 Electronic Outside Micrometer with a resolution of 0.001 mm. Compared to the original designed build height of 50.8 mm shown in the STL, approximately 15 layers of material at the bottom of the part (1.2 % of the part) is lost when the part is removed from the substrate.

Each scanned geometry from the point cloud data is first shifted and rotated to be aligned with its STL as reference, by which the normal displacements of its outside surface can then be extracted. When the normal displacement is positive (in the same direction as the normal vector \overrightarrow{n} shown in Fig. 15), it indicates normal expansion of the outside surface, whereas negative normal displacement indicates shrinkage.

An average distortion τ with respect to height h, along the sample paths AB and A'B', can be estimated as follows:

$$\tau(h) = |dist(p, p') - w|/2 \tag{9}$$

where dist(p,p') denotes the distance between point p and point p', which are picked respectively from path AB and path A'B' at the same height h; and w denotes the width of the part obtained from its STL.

Fig. 16 plots the normal distortion of the outer wall surface along the sample paths for each of the twin square-canonical parts, obtained from the point cloud data. Note that the rightmost distortion data point in Fig. 16 that can be extracted from the point cloud data corresponds to

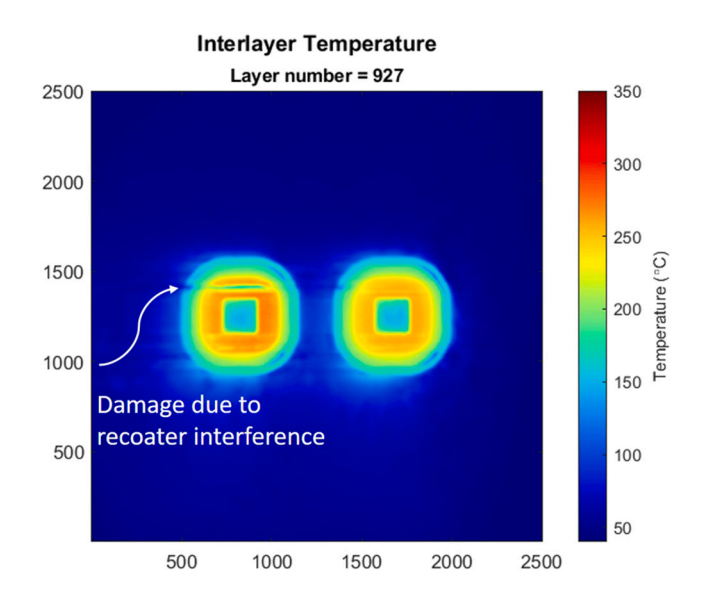


Fig. 17. Thermal imaging at Layer 927 (Method A) indicates recoater interference.

the height value of 50 mm, equivalent to Layer 1264, considering that the height of the part after being cut from the substrate is 50.22 mm.

It can be observed that the two square-canonical parts have a very similar distortion profile with respect to height except near the top of the part, where the left part exhibits increased distortion whereas the distortion in the right part continues to decrease. It is not clear what has caused such sample discrepancy near the top of the final build. Both parts show a drastic change of distortion centered slightly over 40 mm, and such distortion is caused by layer shrinkage as shown in Fig. 15. Noting that the thickness of the outer wall is 2.29 mm, the peak distortion is about 17 % of the thickness of the outer wall and thus is not negligible. Considering the layer thickness of 40 μ m, a distance of 9.7 mm (or 9.3 mm) from the last data point at height of 50 mm in Fig. 16 is equivalent to ~243 layers (or 233 layers) lower than Layer 1264 (corresponding to height value of 50 mm), i.e., at Layer 1021 (or Layer 1031). This indicates that the peak distortion occurs approximately at where the inner and outer walls merge into a single juncture (see Fig. 1).

Recall that the peak interlayer temperature of the inner wall occurs just before Layer 894, where the inner wall surface comes in contact with the support, and the peak interlayer temperature of the outer wall occurs just before Layer 1144, where the inner and outer walls separate again. That is, the peak distortion of the outside wall does not occur at the same layer where the peak interlayer temperature is achieved, providing yet another experimental evidence to demonstrate that part-scale thermal evolution is not a sufficient indicator for post-process distortion.

As seen in Fig. 8, recoater interference, which occurred during the build process, has caused damage to the recoater blade and left horizontal marks on the parts. Recoater interference could be clearly observed as early as Layer 927 from the thermal imaging, as shown in Fig. 17. The study by Peter et al. [39] considered that overheating due to insufficient cooling or insufficient conduction to dissipate heat away from the exposed region could be one contributing factor to recoater interference.

4. Conclusion

This paper conducted an experimental study of the evolution of interlayer temperature distributions during the layer-by-layer L-PBF build process of twin square-canonical parts of Inconel 718. The geometric features of the square-canonical part as well as the location where the support structure comes in contact with the part have led to complex thermal behavior during the build process as well as significant postprocess part distortion, which could lend insight to future part-scale thermo-mechanical simulation tools. Experimental results in this paper show that the interlayer temperature, under which a subsequent new layer is built, has its peak value that is much higher than the preheated substrate temperature under which the first layer of the part is built. As indicated in studies by Chen et al. [7] and Tran et al. [8], significant increase of the layer-wise initial temperature could drastically affect the melt-pool morphology and the design of process-parameters to avoid keyhole melting or to avoid transitioning into keyhole regime. It is expected that the developed in-situ sensing approach for interlayer temperature measurements could be used to obtain feedback for future development of layer-by-layer control of process parameters. This study also shows that the peak distortion on the outside wall of the part is decoupled from the peak interlayer temperature, providing yet another experimental example to demonstrate that part-scale thermal evolution is not a sufficient indicator for post-process distortion. Recoater interference was observed during the build process, and thermo-mechanical simulations will be conducted in the future to elucidate the distortion root cause due to part geometry, support structure, and residual stress. Future work would also investigate potential correlation of part-scale temperature evolution with local microstructures and mechanical properties.

Supplementary data to this article can be found online at https://doi.org/10.1016/j.jmapro.2022.07.026.

Declaration of competing interest

None.

Acknowledgments

This work was supported in part by Autodesk, United States; PA manufacturing fellows program under No. 1060145-406189, United States; and the U.S. National Science Foundation under Grant No. 2015930. We would also like to thank Mr. Corey Dickman and Mr. Peter Coutts from Penn State Applied Research Lab for performing part of the experiments and measurements.

References

[1] Cooke S, Ahmadi K, Willerth S, Herring R. Metal additive manufacturing: technology, metallurgy and modelling. J Manuf Process 2020;57:978–1003.

- [2] Gouge M, Michaleris P. Thermo-mechanical modeling of additive manufacturing. Butterworth-Heinemann; 2017.
- [3] Haley J, Leach C, Jordan B, Dehoff R, Paquit V. In-situ digital image correlation and thermal monitoring in directed energy deposition additive manufacturing. Opt Express 2021;29(7):9927–41.
- [4] Gouge M, Denlinger E, Irwin J, Li C, Michaleris P. Experimental validation of thermo-mechanical part-scale modeling for laser powder bed fusion processes. Addit Manuf 2019;29:100771.
- [5] Li C, Gouge MF, Denlinger ER, Irwin JE, Michaleris P. Estimation of part-to-powder heat losses as surface convection in laser powder bed fusion. Addit Manuf 2019;26: 258–69.
- [6] Promoppatum P, Yao S-C, Pistorius PC, Rollett AD, Coutts PJ, Lia F, Martukanitz R. Numerical modeling and experimental validation of thermal history and microstructure for additive manufacturing of an inconel 718 product. Prog Addit Manuf 2018:3(1):15–32.
- [7] Chen Q, Zhao Y, Strayer S, Zhao Y, Aoyagi K, Koizumi Y, Chiba A, Xiong W, To AC. Elucidating the effect of preheating temperature on melt pool morphology variation in inconel 718 laser powder bed fusion via simulation and experiment. Addit Manuf 2021;37:101642.
- [8] Tran H-C, Lo Y-L, Le T-N, Lau AK-T, Lin H-Y. Multi-scale simulation approach for identifying optimal parameters for fabrication of high-density inconel 718 parts using selective laser melting. Rapid Prototyp J 2021;28(1):109–25.
- [9] Dugast F, Apostolou P, Fernandez A, Dong W, Chen Q, Strayer S, Wicker R, To AC. Part-scale thermal process modeling for laser powder bed fusion with matrix-free method and gpu computing. Addit Manuf 2021;37:101732.
- [10] Yavari MR, Cole KD, Rao P. Thermal modeling in metal additive manufacturing using graph theory. J Manuf Sci Eng 2019;141(7):071007.
- [11] Papadakis L, Loizou A, Risse J, Schrage J. Numerical computation of component shape distortion manufactured by selective laser melting. Procedia Cirp 2014;18: 90-5.
- [12] Hodge N, Ferencz R, Solberg J. Implementation of a thermomechanical model for the simulation of selective laser melting. Comput Mech 2014;54(1):33–51.
- [13] Zaeh MF, Branner G. Investigations on residual stresses and deformations in selective laser melting. Prod Eng 2010;4(1):35–45.
- [14] Zhang W, Tong M, Harrison NM. Resolution, energy and time dependency on layer scaling in finite element modelling of laser beam powder bed fusion additive manufacturing. Addit Manuf 2019;28:610–20.
- [15] Raplee J, Plotkowski A, Kirka MM, Dinwiddie R, Okello A, Dehoff RR, Babu SS. Thermographic microstructure monitoring in electron beam additive manufacturing. Sci Rep 2017;7:43554.
- [16] Bartlett JL, Heim FM, Murty YV, Li X. In situ defect detection in selective laser melting via full-field infrared thermography. Addit Manuf 2018;24:595–605.
- [17] Baumgartl H, Tomas J, Buettner R, Merkel M. A deep learning-based model for defect detection in laser-powder bed fusion using in-situ thermographic monitoring. Prog Addit Manuf 2020:1–9.
- [18] Krauss H, Eschey C, Zaeh M. Thermography for monitoring the selective laser melting process. In: Proceedings of the solid freeform fabrication symposium; 2012. p. 999–1014.
- [19] Krauss H, Zeugner T, Zaeh MF. Thermographic process monitoring in powderbed based additive manufacturing. In: AIP conference proceedings. vol. 1650. American Institute of Physics; 2015. p. 177–83.
- [20] Lane B, Moylan S, Whitenton EP, Ma L. Thermographic measurements of the commercial laser powder bed fusion process at NIST. Rapid Prototyp J 2016;22(5): 778–87
- [21] Montazeri M, Rao P. Sensor-based build condition monitoring in laser powder bed fusion additive manufacturing process using a spectral graph theoretic approach. J Manuf Sci Eng 2018;140(9).
- [22] Foster S, Carver K, Dinwiddie R, List F, Unocic K, Chaudhary A, Babu S. Process-defect-structure-property correlations during laser powder bed fusion of alloy 718: role of in situ and ex situ characterizations. Metall Mater Trans A 2018;49(11): 5775–98.
- [23] Grasso M, Demir A, Previtali B, Colosimo B. In situ monitoring of selective laser melting of zinc powder via infrared imaging of the process plume. Robot Comput-Integr Manuf 2018;49:229–39.
- [24] Heigel JC, Lane BM, Levine LE. In situ measurements of melt-pool length and cooling rate during 3d builds of the metal am-bench artifacts. Integr Mater Manuf Innov 2020;9(1):31–53.
- [25] Lough CS, Wang X, Smith CC, Landers RG, Bristow DA, Drallmeier JA, et al. Correlation of swir imaging with LPBF 304l stainless steel part properties. Addit Manuf 2020;35:101359.
- [26] Paulson NH, Gould B, Wolff SJ, Stan M, Greco AC. Correlations between thermal history and keyhole porosity in laser powder bed fusion. Addit Manuf 2020;34: 101213.
- [27] Mahmoudi M, Ezzat AA, Elwany A. Layerwise anomaly detection in laser powder-bed fusion metal additive manufacturing. J Manuf Sci Eng 2019;141(3):031002.
- [28] Mohr G, Altenburg SJ, Ulbricht A, Heinrich P, Baum D, Maierhofer C, Hilgenberg K. In-situ defect detection in laser powder bed fusion by using thermography and optical tomography—comparison to computed tomography. Metals 2020;10(1):103.
- [29] Williams RJ, Piglione A, Rønneberg T, Jones C, Pham M-S, Davies CM, Hooper PA. In situ thermography for laser powder bed fusion: effects of layer temperature on porosity, microstructure and mechanical properties. Addit Manuf 2019;30:100880.
- [30] Reza Yavari M, Williams RJ, Cole KD, Hooper PA, Rao P. Thermal modeling in metal additive manufacturing using graph theory: experimental validation with laser powder bed fusion using in situ infrared thermography data. J Manuf Sci Eng 2020;142(12):121005.

- [31] Aermica makes 4026: development of distortion prediction and compensation methods for metal powder-bed am. https://www.americamakes.us/portfolio/4026-development-distortion-prediction-compensation-methods-metal-powder-bed/.
- [32] Sakuma F, Hattori S. Establishing a practical temperature standard by using silicon narrow-band radiation thermometer. In: Temperature, its measurement and control in science and industry; 1982. p. 5.
- [33] Zhang Y, Lu F, Deng T, Shu S, Zhang Y, Zhang T, Lang X. Normal spectral emissivity measurement of graphite in the temperature range between 200 c and 500 c. Fusion Eng Des 2022;175:112998.
- [34] Quinn T. The calculation of the emissivity of cylindrical cavities giving near black-body radiation. Br J Appl Phys 1967;18(8):1105.
- [35] Bergman TL, Incropera FP, DeWitt DP, Lavine AS. Fundamentals of heat and mass transfer. John Wiley & Sons; 2011.
- [36] Dinwiddie RB, Kirka M, Lloyd P, Dehoff R, Lowe L, Marlow G. Calibrating ir cameras for in-situ temperature measurement during the electron beam melt processing of inconel 718 and ti-al6-v4. In: Thermosense: thermal infrared applications XXXVIII. vol. 9861. International Society for Optics and Photonics; 2016. p. 986107.
- [37] Lane B, Whitenton E, Madhavan V, Donmez A. Uncertainty of temperature measurements by infrared thermography for metal cutting applications. Metrologia 2013;50(6):637.
- [38] FARO. Laser trackers: defining accuracy. Lake Mary, FL: April; 2017.
- [39] Peter N, Pitts Z, Thompson S, Saharan A. Benchmarking build simulation software for laser powder bed fusion of metals. Addit Manuf 2020;36:101531.